ICAS 2021 SHANGHAI
International Council of the Aeronautical Sciences
32nd Congress of the International Council of the Aeronautical Sciences
September 6-10, 2021
Pudong Shangri-La, Shanghai, China

A COMPREHENSIVE FRAMEWORK FOR THE COUPLED NONLINEAR AEROELASTIC AND FLIGHT DYNAMIC ANALYSES OF HIGHLY FLEXIBLE AIRCRAFT

Zhang Chi[1], Li Xuefeng[1], Chen Jiawen[1], Zhou Zhou[2] & Qiao Lina[2]

[1]Xi'an Modern Control Technology Research Institute
[2]Northwestern Polytechnical University

Abstract

A comprehensive framework to model and analyze the coupled nonlinear aeroelasticity and flight dynamics of highly flexible aircraft is presented. The methodology is based on the dynamics of 3-D co-rotational beams. The coupling of axial, bending and torsional effects is added to the stiffness and mass matrices of Euler-Bernoulli beam to capture the most relevant characteristics of real wing structure. Finite-state aerodynamic model is coupled with the structural model to simulate the unsteady aerodynamics. And the full-wavelength 1-cos time-varying discrete gust model with spatial distribution is proposed and adopted. A scheme of mixed end-point and mid-point time-marching algorithms is proposed and applied into the implicit predictor-corrector integration, so as to improve the calculation efficiency and accuracy. The ground, body and airflow axes for flight dynamics are re-defined by elemental ones of structural dynamics, followed by the redefinitions of local Euler angles and airflow angles of each element. The framework can be used for quick analyses of flexible aircraft in conceptual and preliminary design phases, including linear and nonlinear trim, aerodynamic load estimation, stability assessment, time-domain simulations and flight performance evaluations. With the framework and calculation program proposed in this paper, the process and internal mechanism of the disintegration mishap of Helios Prototype is revealed.

Keywords: Highly flexible aircraft; Nonlinear aeroelasticity; Flight dynamics; Nonlinear trim; Gust response

1. Introduction

High-altitude long-endurance (HALE) aircraft, especially the solar-powered aircraft, which are being considered for aerial reconnaissance, long-time surveillance, environmental sensing, and communication relays, have been the topic of modern flying vehicles [1].

However, the long and slender wings of HALE aircraft inherently have relatively low structural stiffness, which gives rise to large geometrically nonlinear deformations during normal flights. The aerodynamics, inertia distributions, even the thrust directions could be affected significantly, resulting in the changes of trim conditions, flight stabilities and the overall aeroelastic characteristics of the whole aircraft. Traditional static or dynamic models which based on rigid body or linear elasticity assumptions cannot accurately describe the nonlinear deformations and complex coupling of flight dynamics and aerolesticity. The mishap of Helios Prototype is a typical result brought by the complex interactions among multiple disciplines and the lack of adequate analysis tools [2].

Therefore, coupled models and analysis frameworks that can accurately assess the flight performances of a highly deformed flexible aircraft, and can fully account for the coupling between flight dynamics and both structural nonlinearity and unsteady aerodynamics, are of paramount importance in the analysis and design of highly flexible aircraft [3, 4, 5, 6].

In order to investigate the nonlinear aeroelastic responses, trim solutions and flight stability of a complete highly flexible aircraft, Patil [7, 8] and Hodges [9] developed an analysis package named NATASHA (Nonlinear Aeroelastic Trim and Stability of HALE Aircraft). In their framework, the 2-D Peters' finite state unsteady aerodynamic model is used to calculate the aerodynamic loads, and

geometrically exact fully intrinsic equations are used to model the highly flexible structure. Their researches on a typical flexible flying-wing aircraft show that there are significant differences in flight dynamic characteristics between the deformed and undeformed ones.

A nonlinear aeroelastic simulation toolbox named UM/NAST (The University of Michigan's Nonlinear Aeroelastic Simulation Toolbox) was developed by Cesnik [10] and perfected by Shearer [11, 12] and Su [13], etc., aiming at the investigations of dynamic aeroelastic responses coupled with flight dynamics of highly flexible aircraft. Their analyses are based on the strain-based nonlinear beams and Peters' 2-D aerodynamic model. Two simplified models that can take the effects of skin wrinkling and aerodynamic stall into consideration are added in their framework.

A simulation framework called SHARP (Simulation of High-Aspect-Ratio Planes) was developed by Palacios and his co-workers [14, 15, 16] to study the dynamic characteristics of highly flexible aircraft with large deformations. The displacement-based nonlinear dynamic formulations coupled with an unsteady vortex lattice aerodynamic model are employed to capture the large deformations and nonlinear responses of the flexible aircraft. With the computation of nonlinear static trim parameters and dynamic responses to maneuver and gust loads, this framework can be used to conduct stability analyses, dynamic response simulations, flutter suppressions, and gust load alleviations.

In most researches, the geometrically exact intrinsic beam proposed by Hodges and strain-based nonlinear beam proposed by Cesnik have been frequently used in the modeling of highly flexible wings. However, the displacement-based models, which are more intuitive and can be easily transported to the existing finite element programs, have rarely been utilized. As for the coupling between flight dynamics and aeroelasticity, many researches adopt the mean axes or its ramifications [17, 18], which assume that the elastic deformations are small, and essentially still being the 6-DOF formulation. Even in those approaches in which large deformations are considered, the Euler angles and airflow angles are not defined locally, resulting in the costs of coordinate transformations of displacements and velocities between global and local frames.

The main contribution of this paper, which perfects the foundational work of forerunners, is to propose a new and more comprehensive framework to model and analyze the coupled nonlinear aeroelasticity and flight dynamics of highly flexible aircraft, aimed at the requirements of time-domain simulations and performance evaluations in the preliminary design phase of HALE aircraft.

The starting point of this framework is the dynamics of 3-D co-rotational nonlinear beam model, which can capture the nonlinear deformations and rigid-body motions in a quick and computationally effective way. The coupling between axial, bending and torsional effects that often arise in wings is added to the traditional Euler-Bernoulli beams in order to capture some of the most relevant characteristics of real wing structure.

A mixed time-marching algorithm is proposed and applied into the implicit predictor-corrector integration scheme for the first time, in which the end-point algorithm is used in the predictor step for efficiency and mid-point algorithm with numerical damping in corrector step for energy conserving and computation accuracy and stability. By this means, the time step of nonlinear numerical integration can be extended to as long as 0.1 second and the Newton-Raphson correction will converge in no more than 5 iterations with a tolerance of displacement of 1×10^{-6}.

To couple the flight dynamics with nonlinear aeroelasticity in a more intuitive and straightforward way, the ground, body and airflow axes for flight dynamics are re-defined analogously to the reference frames for structural dynamics at the element level, followed by the redefinitions of local Euler angles and airflow angles of each element. With all the variables defined in local reference systems, the computational costs of coordinate transformations can be reduced, and the efficiency in solution improved.

In the nonlinear trim of a complete flexible aircraft, the Newton-Raphson method is implemented with the forming of Jacobian matrix. And a full-wavelength 1-cos time-varying discrete gust model with spatial distribution is proposed and adopted.

With the proposed framework, numerical studies based on a representative benchmark are conducted and carefully compared with published literature. Followed by the process and internal mechanism of the disintegration mishap of Helios Prototype been revealed by this calculation framework.

2. Theoretical Modeling

2.1 Co-rotation Based Geometrically Nonlinear Structural Model

In the co-rotational formulation, the rigid-body motions are separated from the strain-producing deformations at the local element level. Beams are assumed to be linearly elastic, undergoing large translations and rotations but small strains, and the internal element behavior of a beam is linear, whereas nonlinearity is introduced via the co-rotational technique.

The kinematics and statics of 3-D co-rotational beams were presented in the previous work of the authors [19, 20], where the local and global degrees of freedom, nodal and elemental reference systems, tangential transformation matrix $\mathbf{T}$, material stiffness matrix, geometric stiffness matrix $\mathbf{K}_{t\sigma}$, and static tangent stiffness matrix $\mathbf{K}_{t,stat}$ are defined.

2.2 End-Point Algorithm

The discretized dynamic equilibrium equation at the end of $n+1$ time step is given by:

$$\mathbf{q}_{i,n+1}+\mathbf{q}_{mas,n+1}-\mathbf{q}_{e,n+1}=\mathbf{0} \tag{1}$$

where $\mathbf{q}_{i,n+1}$, $\mathbf{q}_{mas,n+1}$ and $\mathbf{q}_{e,n+1}$ are, respectively, the nodal internal, inertial and external force vectors at time $n+1$.

$\mathbf{q}_{mas}$ can be expressed as:

$$\mathbf{q}_{mas}=\mathbf{U}_e^*\mathbf{f}_{iner}=\mathbf{U}_e^*(\mathbf{M}\mathbf{U}_0^*\ddot{\mathbf{p}}+\frac{l}{12}\tilde{\mathbf{f}}) \tag{2}$$

where

$$\mathbf{U}_e^*=diag(\mathbf{U}_0,\mathbf{U}_e,\mathbf{U}_0,\mathbf{U}_e)\quad \mathbf{U}_0^*=diag(\mathbf{U}_0^T,\mathbf{I}_{3\times3},\mathbf{U}_0^T,\mathbf{I}_{3\times3}) \tag{3}$$

$$\tilde{\mathbf{f}}=\frac{l}{12}\begin{bmatrix}\mathbf{0}_{3\times1}\\ 3\mathbf{S}(\mathbf{w}_1)\mathbf{I}_\rho\mathbf{w}_1+\mathbf{S}(\mathbf{w}_1)\mathbf{I}_\rho\mathbf{w}_2+\mathbf{S}(\mathbf{w}_2)\mathbf{I}_\rho\mathbf{w}_1+\mathbf{S}(\mathbf{w}_2)\mathbf{I}_\rho\mathbf{w}_2\\ \mathbf{0}_{3\times1}\\ \mathbf{S}(\mathbf{w}_1)\mathbf{I}_\rho\mathbf{w}_1+\mathbf{S}(\mathbf{w}_1)\mathbf{I}_\rho\mathbf{w}_2+\mathbf{S}(\mathbf{w}_2)\mathbf{I}_\rho\mathbf{w}_1+3\mathbf{S}(\mathbf{w}_2)\mathbf{I}_\rho\mathbf{w}_2\end{bmatrix} \tag{4}$$

where l is the length of element; $\mathbf{M}$ is the consistent mass matrix; $\mathbf{I}_\rho$ is the tensor of mass moment of inertia; $\mathbf{w}_i$ is the vector of angular velocity at node i in the body-attached elemental frame $\mathbf{U}_e$; and $\mathbf{S}(\cdot)$, the 3×3 skew-symmetric matrix. $\ddot{\mathbf{p}}$ is the vector of nodal accelerations, whose translational components are defined in global reference system $\mathbf{U}_g$ and rotational ones are given in the body-attached frame $\mathbf{U}_e$.

To solve such a system of algebraic non-linear equations with Newton-Raphson method, it is necessary to compute the variations of vectors $\mathbf{q}_{i,n+1}$ and $\mathbf{q}_{mas,n+1}$ to take into account the contributions of internal and inertial forces to the generalized tangent stiffness matrix (details on the derivation of $\delta\mathbf{q}_{i,n+1}$, which leads to the static tangent stiffness matrix $\mathbf{K}_{t,stat}$, are given in Refs. [21] and [22]).

The variation of $\mathbf{q}_{mas,n+1}$ can be expressed as:

$$\delta\mathbf{q}_{mas,n+1}=\mathbf{K}_{t,mas}\delta\mathbf{p}=(\mathbf{K}_{mas1}+\mathbf{K}_{mas2}+\mathbf{K}_{mas3})\delta\mathbf{p} \tag{5}$$

where $\delta\mathbf{p}$ is the variation of the global generalized displacement $\mathbf{p}$. The full expressions of the matrices $\mathbf{K}_{mas1}$, $\mathbf{K}_{mas2}$ and $\mathbf{K}_{mas3}$ are given as:

$$\mathbf{K}_{mas1}=\begin{bmatrix}\mathbf{0}_{4\times12}\\ \mathbf{f}_{iner,4}[-\mathbf{A},\mathbf{0}_{3\times3},\mathbf{A},\mathbf{0}_{3\times3}]+\mathbf{f}_{iner,5}[\mathbf{L}(\mathbf{r}_2)]^T+\mathbf{f}_{iner,6}[\mathbf{L}(\mathbf{r}_3)]^T\\ \mathbf{0}_{4\times12}\\ \mathbf{f}_{iner,10}[-\mathbf{A},\mathbf{0}_{3\times3},\mathbf{A},\mathbf{0}_{3\times3}]+\mathbf{f}_{iner,11}[\mathbf{L}(\mathbf{r}_2)]^T+\mathbf{f}_{iner,12}[\mathbf{L}(\mathbf{r}_3)]^T\end{bmatrix} \tag{6}$$

$$\mathbf{K}_{mas2}=\frac{1}{\beta\Delta t^2}\mathbf{U}_e^*\mathbf{M}\mathbf{D} \tag{7}$$

$$\mathbf{K}_{mas3}=\frac{\gamma l\mathbf{U}_e^*}{12\beta\Delta t}\begin{bmatrix}\mathbf{0}&\mathbf{0}&\mathbf{0}&\mathbf{0}\\ \mathbf{0}&3\mathbf{K}_1+\mathbf{K}_2&\mathbf{0}&\mathbf{K}_1+\mathbf{K}_2\\ \mathbf{0}&\mathbf{0}&\mathbf{0}&\mathbf{0}\\ \mathbf{0}&\mathbf{K}_1+\mathbf{K}_2&\mathbf{0}&\mathbf{K}_1+3\mathbf{K}_2\end{bmatrix}\mathbf{D} \tag{8}$$

where β, γ and Δt are, respectively, the time integration parameters of Newmark method and time step.

$$\mathbf{D} = diag\left(\mathbf{U}_0^T,\ \mathbf{U}_{1,n}^T\mathbf{H}^{-1}(\Delta\psi_1),\ \mathbf{U}_0^T,\ \mathbf{U}_{2,n}^T\mathbf{H}^{-1}(\Delta\psi_2)\right) \quad \mathbf{K}_i = \mathbf{S}(\mathbf{w}_i)\mathbf{I}_\rho - \mathbf{S}(\mathbf{I}_\rho\mathbf{w}_i), \quad (i=1,2) \tag{9}$$

where $\mathbf{U}_{i,n}$ is the nodal reference frame of node i at time n. $\mathbf{H}^{-1}(\cdot)$ is the matrix that relates the non-additive pseudo-vector changes to the additive ones $\Delta\psi_i$. Matrices $\mathbf{A}$, $\mathbf{L}(\mathbf{r}_2)$ and $\mathbf{L}(\mathbf{r}_3)$ depend on the definition of the co-rotational element frame. They are all given in Refs. [21] and [22].

2.3 Mid-Point Algorithm

The dynamic equilibrium equation of the mid-point algorithm is given by:

$$\mathbf{g}_m = \mathbf{q}_{e,m} - \mathbf{q}_{i,m} - \mathbf{q}_{mas,m} = \mathbf{0} \tag{10}$$

where $\mathbf{q}_{e,m}$, $\mathbf{q}_{i,m}$ and $\mathbf{q}_{mas,m}$ are vectors of mid-point external, internal and inertial nodal forces.
The mid-point inertial force vector in present framework is defined as:

$$\mathbf{q}_{mas,m} = \frac{1}{\Delta t}(\mathbf{U}_{e,n+1}^*\mathbf{M}\mathbf{U}_0^*\dot{\mathbf{p}}_{n+1} - \mathbf{U}_{e,n}^*\mathbf{M}\mathbf{U}_0^*\dot{\mathbf{p}}_n) \tag{11}$$

where $\dot{\mathbf{p}}_n$ and $\dot{\mathbf{p}}_{n+1}$ are, respectively, the vectors of nodal velocities at step n and $n+1$, whose translational components are defined in the global reference system $\mathbf{U}_g$ and the rotational ones in the body-attached frame $\mathbf{U}_e$.
The nodal external and internal forces acting during the time step are represented by their mid-point values:

$$\mathbf{q}_{e,m} = \frac{\mathbf{q}_{e,n} + \mathbf{q}_{e,n+1}}{2} \tag{12}$$

$$\mathbf{q}_{i,m} = (\frac{\mathbf{T}_n + \mathbf{T}_{n+1}}{2})^T \frac{\mathbf{q}_{il,n} + \mathbf{q}_{il,n+1}}{2} \tag{13}$$

where $\mathbf{q}_{il,n}$ and $\mathbf{q}_{il,n+1}$ are the local nodal internal forces at time n and $n+1$, respectively, and the matrices $\mathbf{T}_n$ and $\mathbf{T}_{n+1}$ are the corresponding tangential transformation matrices.
The inertial contribution to the effective stiffness matrix is obtained from the variation of Eq.(11):

$$\delta\mathbf{q}_{mas,m} = \mathbf{K}_{tmas,m}\delta\mathbf{p} = (\mathbf{K}_{mas1,m} + \mathbf{K}_{mas2,m})\delta\mathbf{p} \tag{14}$$

The full expressions of the matrices $\mathbf{K}_{mas1,m}$ and $\mathbf{K}_{mas2,m}$ are given as:

$$\mathbf{K}_{mas1,m} = \begin{bmatrix} \mathbf{0} & \mathbf{0} & \mathbf{0} & \mathbf{0} \\ \mathbf{0} & -\mathbf{S}(\mathbf{U}_{1,n+1}\mathbf{M}_r(2\mathbf{w}_1+\mathbf{w}_2)) & \mathbf{0} & \mathbf{0} \\ \mathbf{0} & \mathbf{0} & \mathbf{0} & \mathbf{0} \\ \mathbf{0} & \mathbf{0} & \mathbf{0} & -\mathbf{S}(\mathbf{U}_{2,n+1}\mathbf{M}_r(\mathbf{w}_1+2\mathbf{w}_2)) \end{bmatrix} \tag{15}$$

$$\mathbf{K}_{mas2,m} = \frac{2}{\Delta t}\mathbf{U}_{e,n+1}^*\mathbf{M}\mathbf{D} \tag{16}$$

where $\mathbf{M}_r = \frac{l}{6}\mathbf{I}_\rho$.
The mid-point static tangential stiffness matrix $\mathbf{K}_{tstat,m}$ is given by:

$$\delta\mathbf{q}_{i,m} = \mathbf{K}_{tstat,m}\delta\mathbf{p} = \frac{(\mathbf{T}_n+\mathbf{T}_{n+1})^T}{2}\frac{\mathbf{K}_l}{2}\mathbf{T}_{n+1}\delta\mathbf{p} + \frac{1}{2}\mathbf{K}_{t\sigma}(\frac{\mathbf{q}_{il,n}+\mathbf{q}_{il,n+1}}{2})\delta\mathbf{p} \tag{17}$$

which comes from the variation of Eq.(11). $\mathbf{K}_l$ is the local linear stiffness matrix, and the geometric stiffness matrix $\mathbf{K}_{t\sigma}$ takes the identical form to that of the statics [20].
The effective tangential stiffness matrix of the mid-point algorithm is then expressed as the sum of the static term $\mathbf{K}_{tstat,m}$ and the dynamic term $\mathbf{K}_{tmas,m}$:

$$\mathbf{K}_{t,m} = \mathbf{K}_{tstat,m} + \mathbf{K}_{tmas,m} \tag{18}$$

2.4 Mixed Time-Marching Integration Algorithm

The mixed time-marching algorithm is proposed and applied into the implicit predictor-corrector time integration scheme for the first time, in which the end-point algorithm is used in the predictor step for efficiency and mid-point algorithm with numerical damping in corrector step for energy conserving and computation accuracy and stability.

2.4.1 Predictor Step with End-Point Algorithm

Assume all of the required information is available at step n, we can adopt the standard Newmark interpolation to get the vectors of velocity and acceleration at time $n+1$, then the corresponding internal and inertial forces. Here we use the HHT-α time integration scheme, so the end-point dynamic equilibrium equation (Eq.(1)) is now expressed as:

$$(1+\alpha)(\mathbf{q}_{i,n+1}-\mathbf{q}_{e,n+1})-\alpha(\mathbf{q}_{i,n}-\mathbf{q}_{e,n})+\mathbf{q}_{mas,n+1}=\mathbf{0} \tag{19}$$

The values at time n and $n+1$ are then substituted into Eq.(19), which finally leads to a set of equations of the form:

$$\Delta\bar{\mathbf{q}}=\bar{\mathbf{K}}_{t,n}\Delta\mathbf{p} \tag{20}$$

where

$$\bar{\mathbf{K}}_{t,n}=(1+\alpha)\mathbf{K}_{t,stat}+\mathbf{K}_{mas1}+\frac{1}{\beta\Delta t^2}\mathbf{K}_{mas2}+\frac{\gamma}{\beta\Delta t}\mathbf{K}_{mas3} \tag{21}$$

is the equivalent dynamic tangent stiffness matrix, which includes contributions from both the internal and inertial terms.

$$\Delta\bar{\mathbf{q}}=(1+\alpha)\mathbf{q}_{e,n+1}-\alpha\mathbf{q}_{e,n}-\mathbf{q}_{i,n}-\mathbf{q}_{mas,n}+\mathbf{K}_{mas2}\frac{1}{\beta\Delta t}(\dot{\mathbf{p}}_n+\frac{\Delta t}{2}\ddot{\mathbf{p}}_n)+\mathbf{K}_{mas3}[\frac{\gamma}{\beta}\dot{\mathbf{p}}_n-\Delta t(1-\frac{\gamma}{2\beta})\ddot{\mathbf{p}}_n] \tag{22}$$

is the equivalent incremental loads, and $\Delta\mathbf{p}$ is the predicted incremental displacement from time step n to $n+1$.

2.4.2 Corrector Step with Mid-Point Algorithm

Having solved Eq.(20) for $\Delta\mathbf{p}$, the vectors of displacement, velocity and acceleration at step $n+1$ can be obtained by the Newmark interpolation relations; the corresponding internal and inertial force vectors are to be obtained successively.

The values at the mid-point can be interpolated and then substituted into the mid-point dynamic equilibrium equation (Eq.(10)), which will, in general, lead to a residual $\mathbf{g}_m$ that is not zero. Therefore, a standard process of Newton-Raphson (or modified Newton-Raphson or quasi-Newton) iteration is to be applied, which gives:

$$\mathbf{g}_m=\bar{\mathbf{K}}_{t,m}\delta\mathbf{p} \tag{23}$$

where

$$\bar{\mathbf{K}}_{t,m}=\mathbf{K}_{tstat,m}+\frac{1}{\Delta t}(\mathbf{K}_{mas1,m}+\mathbf{K}_{mas2,m}) \tag{24}$$

is the equivalent dynamic tangent stiffness matrix of mid-point algorithm. Note it takes the different form to that previously given for the predictor step.

By solving Eq.(23), the improvement $\delta\mathbf{p}$ to $\mathbf{p}_{n+1}$ can be obtained, so that:

$$\mathbf{p}_{n+1,new}=\mathbf{p}_{n+1,old}+\delta\mathbf{p} \tag{25}$$

The more detailed descriptions of 3-D formulations for a spatial beam and the numerical implementations of the rotational updates, as well as the overall solution strategy, can be found in the co-rotational nonlinear finite element literature [23, 24, 22, 25, 26].

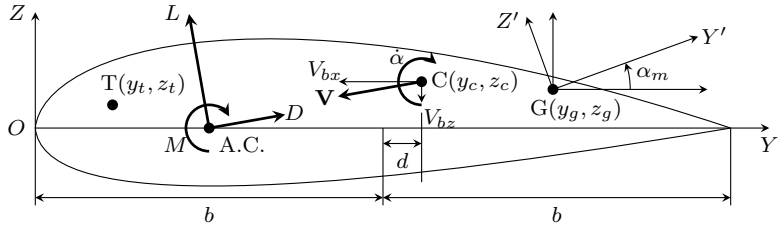

Figure 1 – Beam reference coordinate system.

2.5 Element Stiffness and Mass Matrices

The coupling between axial, bending and torsional effects is added into the element stiffness and mass matrices in the present framework by considering the flap-torsion (FT), lag-torsion (LT) and axial-torsion (AT) cross-stiffness properties in the stiffness matrix, and dynamic coupling terms between torsion and bending in the mass matrix.

As illustrated in Figure 1,the element stiffness matrix in the basic coordinate system is given as:

$$\mathbf{k}_o = \mathbf{T}_k^T \mathbf{k}_{el} \mathbf{T}_k \tag{26}$$

where

$$\mathbf{T}_k = \begin{bmatrix} \mathbf{t}_k & \mathbf{0}_{6\times6} \\ \mathbf{0}_{6\times6} & \mathbf{t}_k \end{bmatrix} \quad \mathbf{t}_k = \begin{bmatrix} 1 & 0 & 0 & 0 & z_t & -y_t \\ 0 & 1 & 0 & -z_c & 0 & 0 \\ 0 & 0 & 1 & y_c & 0 & 0 \\ 0 & 0 & 0 & 1 & 0 & 0 \\ 0 & 0 & 0 & 0 & 1 & 0 \\ 0 & 0 & 0 & 0 & 0 & 1 \end{bmatrix} \tag{27}$$

The element stiffness matrix in local axes [27] can be expressed as:

$$\mathbf{k}_{el} = \begin{bmatrix} \mathbf{A} & \mathbf{B}^T \\ \mathbf{B} & \mathbf{C} \end{bmatrix} \tag{28}$$

in which

$$\mathbf{A} = \begin{bmatrix} \frac{EA}{l} & 0 & 0 & \frac{AT}{l} & 0 & 0 \\ 0 & \frac{12EI_z}{l^3} & \frac{12EI_{yz}}{l^3} & 0 & -\frac{6EI_{yz}}{l^2} & \frac{6EI_z}{l^2} \\ 0 & \frac{12EI_{yz}}{l^3} & \frac{12EI_y}{l^3} & 0 & -\frac{6EI_y}{l^2} & \frac{6EI_{yz}}{l^2} \\ \frac{AT}{l} & 0 & 0 & \frac{GJ}{l} & \frac{FT}{l} & -\frac{LT}{l} \\ 0 & -\frac{6EI_{yz}}{l^2} & -\frac{6EI_y}{l^2} & \frac{FT}{l} & \frac{4EI_y}{l} & -\frac{4EI_{yz}}{l} \\ 0 & \frac{6EI_z}{l^2} & \frac{6EI_{yz}}{l^2} & -\frac{LT}{l} & -\frac{4EI_{yz}}{l} & \frac{4EI_z}{l} \end{bmatrix}$$

$$\mathbf{B} = \begin{bmatrix} \frac{-EA}{l} & 0 & 0 & \frac{-AT}{l} & 0 & 0 \\ 0 & \frac{-12EI_z}{l^3} & \frac{-12EI_{yz}}{l^3} & 0 & \frac{6EI_{yz}}{l^2} & \frac{-6EI_z}{l^2} \\ 0 & \frac{-12EI_{yz}}{l^3} & \frac{-12EI_y}{l^3} & 0 & \frac{6EI_y}{l^2} & \frac{-6EI_{yz}}{l^2} \\ \frac{-AT}{l} & 0 & 0 & \frac{-GJ}{l} & \frac{-FT}{l} & \frac{LT}{l} \\ 0 & \frac{-6EI_{yz}}{l^2} & \frac{-6EI_y}{l^2} & \frac{-FT}{l} & \frac{2EI_y}{l} & \frac{-2EI_{yz}}{l} \\ 0 & \frac{6EI_z}{l^2} & \frac{6EI_{yz}}{l^2} & \frac{LT}{l} & \frac{-2EI_{yz}}{l} & \frac{2EI_z}{l} \end{bmatrix}$$

$$\mathbf{C} = \begin{bmatrix} \frac{EA}{l} & 0 & 0 & \frac{AT}{l} & 0 & 0 \\ 0 & \frac{12EI_z}{l^3} & \frac{12EI_y}{l^3} & 0 & \frac{6EI_{yz}}{l^2} & -\frac{6EI_z}{l^2} \\ 0 & \frac{12EI_y}{l^3} & \frac{12EI_y}{l^3} & 0 & \frac{6EI_y}{l^2} & -\frac{6EI_{yz}}{l^2} \\ \frac{AT}{l} & 0 & 0 & \frac{GJ}{l} & \frac{FT}{l} & -\frac{LT}{l} \\ 0 & \frac{6EI_{yz}}{l^2} & \frac{6EI_y}{l^2} & \frac{FT}{l} & \frac{4EI_y}{l} & -\frac{4EI_{yz}}{l} \\ 0 & -\frac{6EI_z}{l^2} & -\frac{6EI_{yz}}{l^2} & -\frac{LT}{l} & -\frac{4EI_{yz}}{l} & \frac{4EI_z}{l} \end{bmatrix}$$

Descriptions of the symbols in Eq.(28) are given in Table 1.

Table 1 – Variables defining stiffness matrix.

Symbol	Description
EA	Axial stiffness
EI_y	Bending stiffness around y axis (flapwise)
EI_z	Bending stiffness around z axis (lagwise)
EI_{yz}	Flap-lag bending stiffness around y and z axes
GJ	Torsional stiffness
AT	Coupled axial-torsional stiffness
FT	Coupled flap-torsional stiffness
LT	Coupled lag-torsional stiffness
l	Length of element

The element mass matrix in the basic coordinate system is:

$$\mathbf{m}_o = \mathbf{T}_m^T \mathbf{Q}_m^T \mathbf{m}_{el} \mathbf{Q}_m \mathbf{T}_m \tag{29}$$

where

$$\mathbf{T}_m = \begin{bmatrix} \mathbf{t}_m & \mathbf{0}_{6\times6} \\ \mathbf{0}_{6\times6} & \mathbf{t}_m \end{bmatrix} \quad \mathbf{t}_m = \begin{bmatrix} 1 & 0 & 0 & 0 & z_g & -y_g \\ 0 & 1 & 0 & -z_c' & 0 & 0 \\ 0 & 0 & 1 & y_c' & 0 & 0 \\ 0 & 0 & 0 & 1 & 0 & 0 \\ 0 & 0 & 0 & 0 & 1 & 0 \\ 0 & 0 & 0 & 0 & 0 & 1 \end{bmatrix} \tag{30}$$

$$\mathbf{Q}_m = \begin{bmatrix} \mathbf{q}_m & \mathbf{0}_{6\times6} \\ \mathbf{0}_{6\times6} & \mathbf{q}_m \end{bmatrix} \quad \mathbf{q}_m = \begin{bmatrix} 1 & 0 & 0 & 0 & 0 & 0 \\ 0 & c(\alpha_m) & s(\alpha_m) & 0 & 0 & 0 \\ 0 & -s(\alpha_m) & c(\alpha_m) & 0 & 0 & 0 \\ 0 & 0 & 0 & 1 & 0 & 0 \\ 0 & 0 & 0 & 0 & c(\alpha_m) & s(\alpha_m) \\ 0 & 0 & 0 & 0 & -s(\alpha_m) & c(\alpha_m) \end{bmatrix} \tag{31}$$

where $c(\alpha_m) = \cos(\alpha_m)$, $s(\alpha_m)\sin(\alpha_m)$, and (y_c', z_c') is the coordinates of shear center (C) in the local reference system for the mass matrix $G_{xy'z'}$. The element mass matrix in local axes can be expressed as:

$$\mathbf{m}_{el} = \begin{bmatrix} \mathbf{A} & \mathbf{B}^T \\ \mathbf{B} & \mathbf{C} \end{bmatrix} \tag{32}$$

in which

$$\mathbf{A} = \begin{bmatrix} \frac{\rho Al}{3} & 0 & 0 & 0 & 0 & 0 \\ 0 & \frac{13\rho Al}{35} & 0 & \frac{7z_c'\rho Al}{20} & 0 & \frac{11\rho Al^2}{210} \\ 0 & 0 & \frac{13\rho Al}{35} & -\frac{7y_c'\rho Al}{20} & -\frac{11\rho Al^2}{210} & 0 \\ 0 & \frac{7z_c'\rho Al}{20} & -\frac{7y_c'\rho Al}{20} & \frac{\rho_t l}{3} & \frac{y_c'\rho Al^2}{20} & \frac{z_c'\rho Al^2}{20} \\ 0 & 0 & -\frac{11\rho Al^2}{210} & \frac{y_c'\rho Al^2}{20} & \frac{\rho Al^3}{105} & 0 \\ 0 & \frac{11\rho Al^2}{210} & 0 & \frac{z_c'\rho Al^2}{20} & 0 & \frac{\rho Al^3}{105} \end{bmatrix}$$

$$\mathbf{B} = \begin{bmatrix} \frac{\rho Al}{6} & 0 & 0 & 0 & 0 & 0 \\ 0 & \frac{9\rho Al}{70} & 0 & \frac{3z_c'\rho Al}{20} & 0 & \frac{13\rho Al^2}{420} \\ 0 & 0 & \frac{9\rho Al}{70} & -\frac{3y_c'\rho Al}{20} & -\frac{13\rho Al^2}{420} & 0 \\ 0 & \frac{3z_c'\rho Al}{20} & -\frac{3y_c'\rho Al}{20} & \frac{\rho_t l}{6} & \frac{y_c'\rho Al^2}{30} & \frac{z_c'\rho Al^2}{30} \\ 0 & 0 & \frac{13\rho Al^2}{420} & -\frac{y_c'\rho Al^2}{30} & -\frac{\rho Al^3}{140} & 0 \\ 0 & -\frac{13\rho Al^2}{420} & 0 & -\frac{z_c'\rho Al^2}{30} & 0 & -\frac{\rho Al^3}{140} \end{bmatrix}$$

$$\mathbf{C} = \begin{bmatrix} \frac{\rho Al}{3} & 0 & 0 & 0 & 0 & 0 \\ 0 & \frac{13\rho Al}{35} & 0 & \frac{7z_c'\rho Al}{20} & 0 & \frac{-11\rho Al^2}{210} \\ 0 & 0 & \frac{13\rho Al}{35} & \frac{-7y_c'\rho Al}{20} & \frac{11\rho Al^2}{210} & 0 \\ 0 & \frac{7z_c'\rho Al}{20} & \frac{-7y_c'\rho Al}{20} & \frac{\rho_t l}{3} & \frac{-y_c'\rho Al^2}{20} & \frac{-z_c'\rho Al^2}{20} \\ 0 & 0 & \frac{11\rho Al^2}{210} & \frac{-y_c'\rho Al^2}{20} & \frac{\rho Al^3}{105} & 0 \\ 0 & \frac{-11\rho Al^2}{210} & 0 & \frac{-z_c'\rho Al^2}{20} & 0 & \frac{\rho Al^3}{105} \end{bmatrix}$$

Descriptions of the symbols in (32) are given in Table 2.

Table 2 – Variables defining mass matrix.

Symbol	Description
ρA	Sectional mass per unit length
ρ_y'	Bending inertia about principal axis y' at G
ρ_z'	Bending inertia about principal axis z' at G
(y_c', z_c')	Position of C referred to $G_{xy'z'}$
ρ_t	$\rho_y' + \rho_z' + (y_c'^2 + z_c'^2)\rho A$

2.6 Coupling of Aeroelasticity and Flight Dynamics

In the present framework, given the spatial locations and orientations of every element, the ground, body and airflow axes for flight dynamics are re-defined analogously to the global and elemental reference frames for structural dynamics at the local element level.

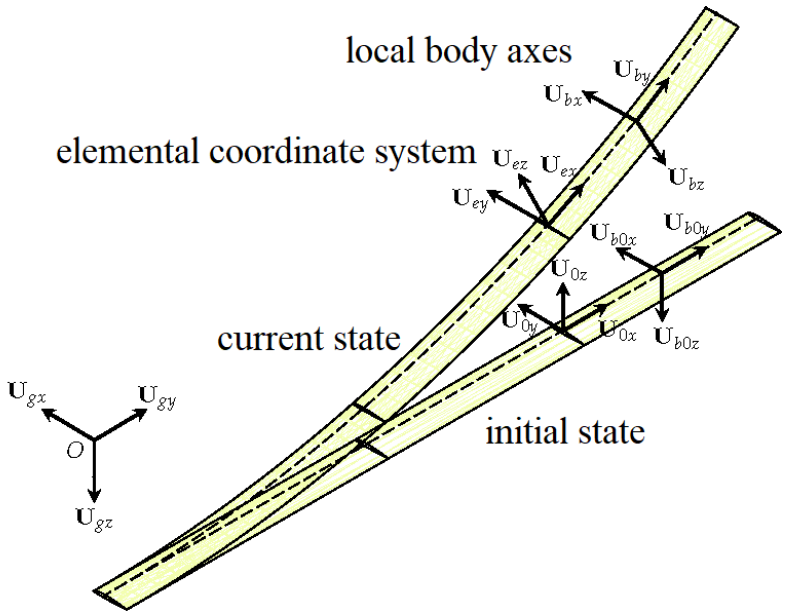

Figure 2 – Global (ground), elemental and body reference frames of the flexible wing.

As illustrated in Figure 2, the ground axes $\mathbf{U}_g$ for flight dynamics is defined to be identical to the global reference frame for aeroelasticity. For each element, there is a body-attached element frame $\mathbf{U}_e$, which translates and rotates continuously with the varying generalized displacements of the element. The element frame $\mathbf{U}_e$ in aeroelasticity is then taken as the body axes $\mathbf{U}_b$ for flight dynamics. Note that, according to the most usual practice in flight dynamics, the x-axis of $\mathbf{U}_b$ is directed to “forward", y-axis is directed to “rightward", and z-axis “downward", while in aeroelasticity, the x-axis of the element frame is preferred to lie along the axial line of the beam, and y, z-axes along the principal axes of inertia. So, the body axes $\mathbf{U}_b$ of a wing element is defined as:

$$\mathbf{U}_b = [\mathbf{U}_{ey}, \mathbf{U}_{ex}, -\mathbf{U}_{ez}] \tag{33}$$

where $\mathbf{U}_{ex}$, $\mathbf{U}_{ey}$ and $\mathbf{U}_{ez}$ are the base vectors of $\mathbf{U}_e$.
With ground axes $\mathbf{U}_g$ and elemental body axes $\mathbf{U}_b$ defined, the Euler angles (roll, pitch, yaw angles) of each element can be defined in the usual way. The translational velocity and acceleration of the element in body axes can be expressed as:

$$\mathbf{V}_b = \mathbf{U}_b^T \mathbf{V}_g; \quad \mathbf{a}_b = \mathbf{U}_b^T \mathbf{a}_g \tag{34}$$

where $\mathbf{V}_g$ and $\mathbf{a}_g$ are, respectively, the inertial velocity and acceleration vectors expressed in the ground or global axes.
The angular velocity and acceleration in body axes can be expressed as:

$$\omega = [w_y, w_x, -w_z]^T; \quad \alpha = [a_y, a_x, -a_z]^T \tag{35}$$

where w_x, w_y, w_z and a_x, a_y, a_z are, respectively, the components of the elemental angular velocity and angular acceleration, which are defined in the element frame $\mathbf{U}_e$, in the light of the co-rotational approach.
With the translational velocity in body axes, the angles of attack and sideslip of an element can be calculated as:

$$\alpha = \arctan(V_{bz}/V_{bx}); \quad \beta = \arcsin(V_{by}/V) \tag{36}$$

where V_{bx}, V_{by}, V_{bz} are the components of $\mathbf{V}_b$; and V is the norm of $\mathbf{V}_b$.

2.7 Peters' Finite State Inflow Model

The unsteady aerodynamic loads used in the current framework are based on the Peters' 2-D finite state inflow theory [28]. The aerodynamic loads per unit span calculated about the aerodynamic center (A.C.) are given as:

$$l_{ac} = \pi\rho b^2(\ddot{z} + \dot{y}\dot{\alpha} - d\ddot{\alpha}) + c_{l\alpha}\rho b\dot{y}^2\left[\frac{\dot{z}}{\dot{y}} + (\frac{1}{2}b - d)\frac{\dot{\alpha}}{\dot{y}} - \frac{\lambda_0}{\dot{y}}\right] + \rho b\dot{y}^2(c_{l0} + c_{l\delta}\delta) \tag{37}$$

$$m_{ac} = -\pi\rho b^3\left[\frac{1}{2}\ddot{z} + \dot{y}\dot{\alpha} + (\frac{1}{8}b - \frac{1}{2}d)\ddot{\alpha}\right] + 2\rho b^2\dot{y}^2(c_{m0} + c_{m\delta}\delta) \tag{38}$$

$$d_{ac} = \rho b\dot{y}^2 c_{d0} \tag{39}$$

where ρ is the air density, b is the semichord, d is the distance of the mid-chord in front of the reference axis (here is the shear center (C)), δ is the trailing-edge flap deflection angle. $c_{l\alpha}$ is the lift curve slope, $c_{l\delta}$ and $c_{m\delta}$ are the lift and moment slopes due to flap deflection, respectively. c_{l0}, c_{m0} and c_{d0} are the lift, moment and drag coefficients for zero angle of attack (AOA), respectively. And λ_0 is the inflow parameter, which accounts for induced flow due to free vorticity.
To transfer the loads from A.C. to the wing reference axis (here is shear center (C)), one may use

$$l_{ra} = l_{ac}; \quad m_{ra} = m_{ac} + (\frac{1}{2}b + d)l_{ac}; \quad d_{ra} = d_{ac} \tag{40}$$

Furthermore, the aerodynamic loads are rotated to the body coordinate system, and then the global coordinate system, which yields:

$$\mathbf{F}_a = \mathbf{U}_e \begin{bmatrix} \cos(\alpha) & 0 & -\sin(\alpha) \\ 0 & 1 & 0 \\ \sin(\alpha) & 0 & \cos(\alpha) \end{bmatrix} \begin{bmatrix} \cos(\beta) & \sin(\beta) & 0 \\ -\sin(\beta) & \cos(\beta) & 0 \\ 0 & 0 & 1 \end{bmatrix} \begin{bmatrix} -d_{ra} \\ 0 \\ -l_{ra} \end{bmatrix} l \tag{41}$$

$$\mathbf{M}_a = \mathbf{U}_e \begin{bmatrix} \cos(\alpha) & 0 & -\sin(\alpha) \\ 0 & 1 & 0 \\ \sin(\alpha) & 0 & \cos(\alpha) \end{bmatrix} \begin{bmatrix} \cos(\beta) & \sin(\beta) & 0 \\ -\sin(\beta) & \cos(\beta) & 0 \\ 0 & 0 & 1 \end{bmatrix} \begin{bmatrix} 0 \\ m_{ra} \\ 0 \end{bmatrix} l \tag{42}$$

where l is the local span, here is the length of the corresponding element.

2.8 Nonlinear Trim of the Flexible Aircraft

The nonlinear trim of the flexible aircraft is performed for zero resultant force and moment of the whole aircraft. A cost function is defined as:

$$f = [\mathbf{F}_R^T, \mathbf{M}_R^T]^T \tag{43}$$

where $\mathbf{F}_R$ and $\mathbf{M}_R$ are the resultant force and moment of the whole aircraft, which can be expressed as:

$$\mathbf{F}_R = \sum_{i=1}^{N} \mathbf{F}_{ai} + \sum_{i=1}^{N} \mathbf{F}_{ti} + \sum_{i=1}^{N} \mathbf{F}_{gi} \tag{44}$$

$$\mathbf{M}_R = \sum_{i=1}^{N} \mathbf{M}_{ai} + \sum_{i=1}^{N} \mathbf{d}_i \times (\mathbf{F}_{ai} + \mathbf{F}_{ti} + \mathbf{F}_{gi}) \tag{45}$$

where $\mathbf{F}_{ai}$, $\mathbf{M}_{ai}$, $\mathbf{F}_{ti}$ and $\mathbf{F}_{gi}$ are, respectively, the aerodynamic force and moment, thrust and gravity acting on the i^{th} node of the aircraft; and $\mathbf{d}_i$ is the distance vector from the moment reference point (e.g. center of gravity or the constraint point of the aircraft) to the i^{th} node.

The cost function f is minimized over the solution space using the body angle of attack α, elevator deflection angle δ, and thrust T. The Newton-Raphson iteration is employed to find the optimal trim parameter S, i.e.

$$S_{k+1} = S_k - \left[\frac{\partial f}{\partial S}\right]_k^{-1} f_k \tag{46}$$

where $S = [\alpha, \delta, T]^T$, and $\left[\frac{\partial f}{\partial S}\right]$ is the Jacobian matrix that relates the resultant force and moment of the whole aircraft with the trim parameters, which is computed numerically trough finite differences as:

$$\mathbf{J}_{ij} \equiv \left[\frac{\partial f_i}{\partial S_j}\right] \simeq \frac{f_i(S + \Delta S_j) - f_i(S)}{\Delta S_j} \tag{47}$$

2.9 Discrete Gust Model with Spatial Distribution

Generally, the wind in atmosphere is random, and its range and speed changes are difficult to accurately describe with a set of simple mathematical expressions. Therefore, a 1-cos gust model with time and space distribution is proposed and adopted in this paper. It forms an ellipse with only vertical upward speed. The gust area is arranged on the flight path. At each moment, the gust speed reaches a given maximum value at the center of the gust and decreases to zero at the edge of the area. The distribution of the gust amplitude in east-west and north-south directions can be different, and the gust velocity at each point in the gust area has the same 1-cos distribution at the same moment.

The gust amplitude at a certain point in the gust area at a certain moment can be calculated by the following equations:

$$A(r, \eta, t) = \frac{1}{2} A_c [1 - \cos(2\pi \frac{t - t_1}{t_g})] \sqrt{(A_E \cos\eta)^2 + (A_N \sin\eta)^2} \tag{48}$$

$$A_E(r) = \sin(\frac{\pi}{2}[1 - (\frac{r}{r_0})^{n_E}]) \tag{49}$$

$$A_N(r) = \sin(\frac{\pi}{2}[1 - (\frac{r}{r_0})^{n_N}]), \quad (0 \le r \le r_0) \tag{50}$$

where the subscripts E and N represent east-west and north-south directions, respectively; A_c is the gust amplitude at the center of the gust; r_0 is the radius of the gust area; r is the distance from a point in the gust area to the center of the gust; η is the horizontal azimuth of a point in the gust area. n_E and n_N are the parameters for adjusting the spatial distribution of the gusts in the east-west and north-south directions, respectively.

Equations 49 and 50 ensure the amplitude be the maximum at the center of the gust while zero at the edge. t_1 is the moment when the gust starts, and t_g is the duration of the gust. Given different parameters, the different time-varying characteristics and different spatial distributions of the discrete gust models can be obtained.

3. Numerical Validation

Validations of the structural static solution under given loads and static aeroelastic responses with different flight conditions, have been presented in the previous work of the authors [19, 20], which will not be repeated here.

To validate the implementation of the coupling of flight dynamics with nonlinear aeroelasticity and the corresponding computing codes, the trim and dynamic responses of a representative highly flexible flying-wing aircraft with a span of 72.8 m, a constant chord of 2.44 m, and a payload varying from 0 to 227 kg on the central pod (Note that the payload is not considered all the mass at the point where the central pod locates; apart from the payload, there is also the structural mass of the central pod itself, which is 27.23 kg.), as shown in Figure 3 and Table 3, are analyzed and compared carefully to the results taken from Patil [9] and Su [13], respectively.

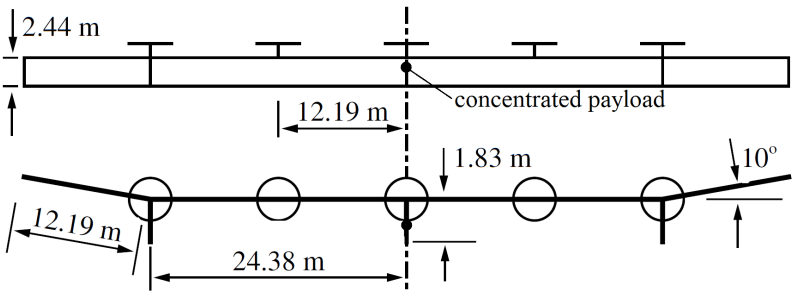

Figure 3 – Geometry of the flying wing model.

Table 3 – Properties of the flying wing (after [13]).

Strucutral Property	Value	Aerodynamic Property	Value
Cross-sectional elastic axis	25% chord from L.E.	$c_{l\alpha}$ for wings (25% chord)	2π
Cross-sectional center of gravity	25% chord from L.E.	$c_{l\delta}$ for wings (25% chord)	1
Torsional stiffness	$1.65301\times10^5\ Nm^2$	c_{d0} for wings (25% chord)	0.01
Bending stiffness	$1.03313\times10^6\ Nm^2$	c_{m0} for wings (25% chord)	0.025
Chordwise bending stiffness	$1.23976\times10^7\ Nm^2$	$c_{m\delta}$ for wings (25% chord)	-0.25
Mass per unit length	8.92898 kg/m	$c_{l\alpha}$ for pods (25% chord)	5
Torsional mass moment of inertia	4.14765 kgm	c_{d0} for pods (25% chord)	0.02
Flatwise bending mass moment of inertia	0.691275 kgm		
Chordwise bending mass moment of inertia	3.45637 kgm		

3.1 Trim Analysis

At the flight speed of 12.2 m/s on sea level, the highly flexible aircraft with the varying concentrated payload is trimmed for zero resultant force and moment. Figure 4 shows the variations of the trimmed AOA, flap deflection angle (assuming constant throughout the span) and thrust per motor with the varying payload. It can be seen that the trim AOA increases with the payload, for the heavier the payload, the higher lift required, and so the higher AOAs. When the concentrated payload increases, the aerodynamic loads get higher, which leads to large bending deformations in the highly flexible wings; and the aircraft turns into a “U” shape as illustrated in Figure 5.

As the aircraft deforms to a “U” shape, the aerodynamic center moves backward, which brings about a pitch-down moment, and the flap deflection decreases to reduce the additional pitch-down moment of the flap.

3.2 Stability Analysis

Time-domain simulations of the nonlinear dynamic responses of the highly flexible aircraft with three different payload masses (122 kg, 152 kg and 227 kg) are performed. The aircraft is initially at its trimmed state; perturbation is introduced by adding a pre-defined flap deflection change: the flap deflection angle ramps linearly up to 5° between 1 and 2 seconds, and then ramps linearly back to its trimmed angle between 2 and 3 seconds, then it keeps constant.

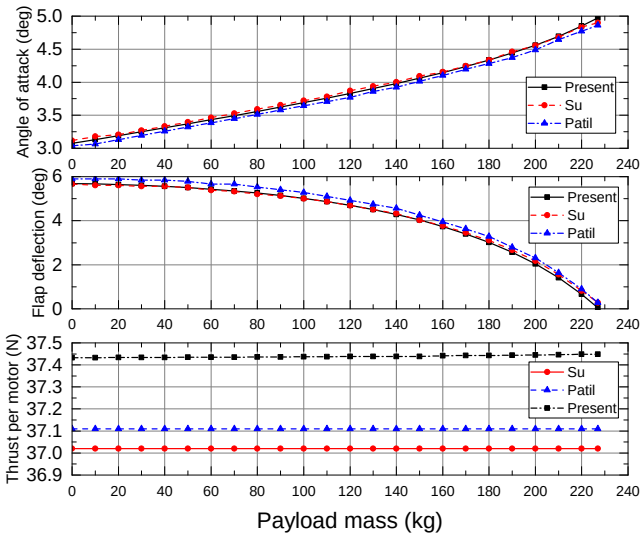

Figure 4 – Trim results of the flying wing with varying payload mass.

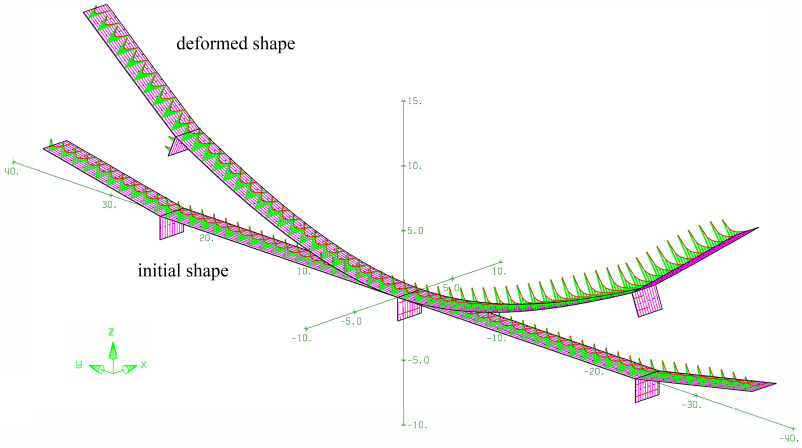

Figure 5 – Initial and deformed shapes with heavy payload.

The simulation is conducted by the direct solution of the complete nonlinear dynamic equations by implicit predictor-corrector schemes with the mixed time-marching algorithms and a time step of up to 0.1 s. Figures 6-8 show the variations of altitude, airspeed, and AOA of the mid-span (the center) of the aircraft, respectively.

It can be seen from Figures 6 and 7 that, with a payload of 122 kg at the central pod, the phugoid mode of the highly flexible aircraft is neutrally stable, for the altitude and airspeed of the vehicle after perturbation oscillate with equal amplitudes. When the payload increases to 152 or 227 kg, the phugoid mode becomes unstable with increasing amplitudes of oscillations: the heavier the payload, the higher frequency and larger amplitude of the oscillation. For the differences between the two results given by Patil [9] and Su [13], Su attributed them to the differences of damping of the models used, which the authors think was not explained precisely. In the opinion of the authors of the present paper, it is more likely to be the difference of payload masses that leads to the different results.

From Figures 6 and 7, the exchange between potential energy and kinetic energy of the highly flexible aircraft can be seen clearly from the out-of-phase variations between the altitudes and airspeeds. Besides, the aircraft altitude loss indicates a loss of energy due to the unstable phugoid mode and constant thrust.

As shown in Figure 8, within several cycles of oscillations, the mid-span (also the whole aircraft) starts to experience very high AOAs in every cycle, which is the inevitable result of the excited unstable phugoid mode.

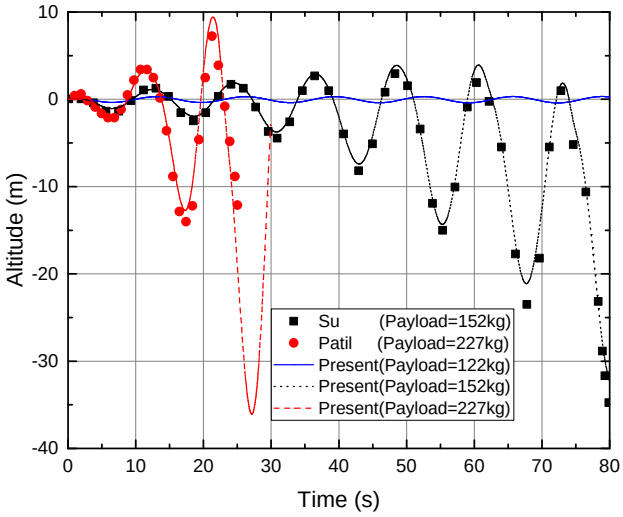

Figure 6 – Altitude of flight with different payload.

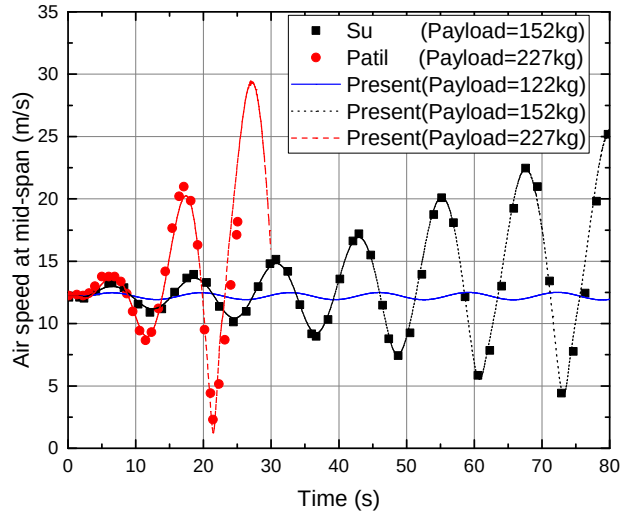

Figure 7 – Airspeed of flight with different payload.

It is to be noted that, since stall is not yet included in the present framework, the results at high AOAs cannot be considered to be the real motion of the aircraft. Once the dynamic stall is included, one would see the different responses at the highest altitudes, where the lift will be insufficient to balance the weight and the aircraft drops with the increase in velocity, resulting in instantaneous higher AOAs. In addition, it can be clearly seen that excellent agreements are made with the results supplied by Patil [9] for 227 kg payload mass and Su [13] for 152 kg payload mass, which demonstrates the validity and accuracy of the presented framework and its corresponding computing codes.

3.3 Mechanism Analysis of the Disintegration of Helios Prototype

As shown in figure 9, the Helios HP03-2 aircraft adopts a high aspect-ratio full-wing layout, with a wingspan of 75.3 m, consisting of 6 segments. The 4 inner segments are straight wings, and the 2 outer ones each have a dihedral of 10°. The chord length of the wing is 2.44 m, and the aspect-ratio is 30.9. Five pods are evenly distributed under the wings. The central pod is equipped with fuel cells and weighs 235.9 kg, and the 4 pods on both sides are equipped with avionics. A hydrogen fuel pod

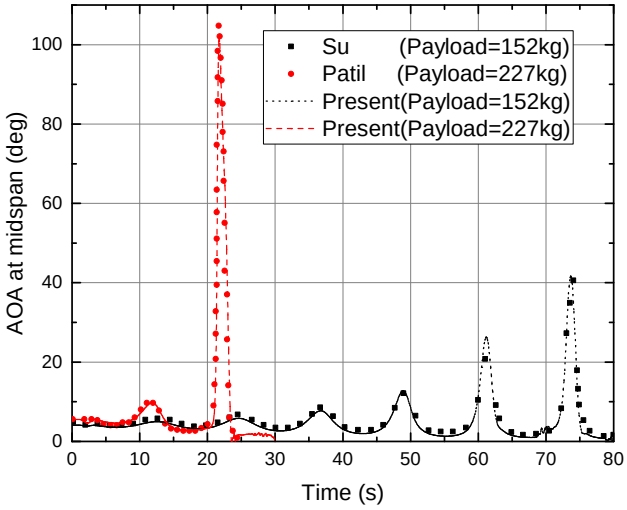

Figure 8 – AOA at mid-span with different payload.

weighing 74.8 kg is installed in the middle of the left and right outer wing sections. After installing hydrogen-oxygen fuel cells and experimental equipment, the take-off weight of the HP03-2 aircraft increased to 1052 kg[2].

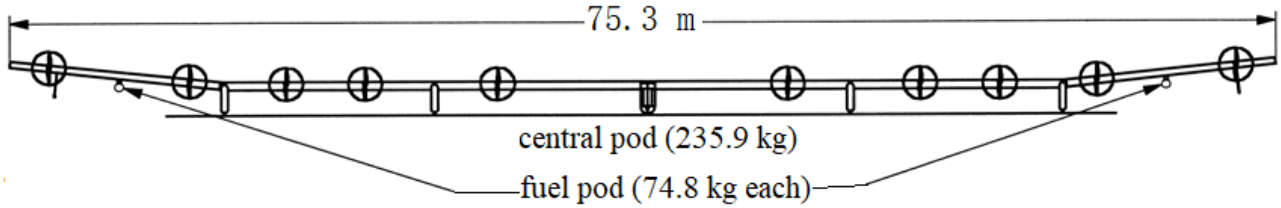

Figure 9 – Helios HP03-2

The geometry, mass distributoin, thrust characteristics and cruising state are set the same as the above-mentioned Helios HP03-2 aircraft. The structural rigidity and cross-sectional aerodynamic coefficients of the wing adopt the parameters of the aforementioned "Helios-like" aircraft. At the initial moment, the aircraft was trimmed at an altitude of 850 m above sea level (atmospheric density of 1.13 kg/m$ˆ3$) and flew straight and level at a speed of 11.6 m/s. At the end of 2 s, an infinite full-wavelength 1-cos discrete gust with an amplitude of 1 m and a duration of 10 s began to be encountered.
The spatial locations and shape, pitch angle and pitch angle rate, airspeeds and overloads of wing tip and root of the "Helios" HP03-2 are illustrated in Figure 10 to Figure 12.

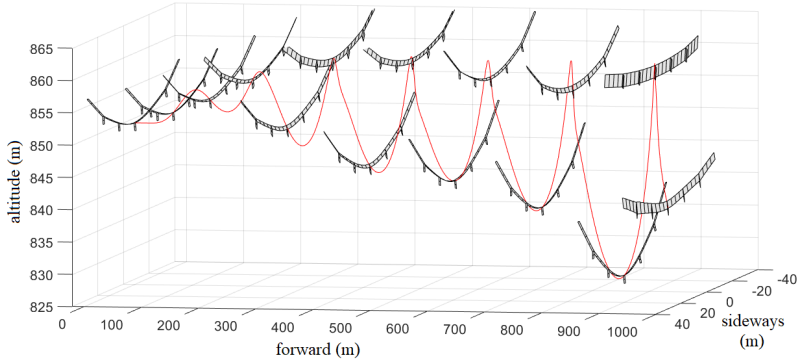

Figure 10 – The position and morphological change of the aircraft

It can be seen from figure 10 that when the plane is flying straight and level, the wing has a certain degree of bending deformation, and the wing tip deflection is about 7 m, which is about 9% of the wingspan. After being affected by the vertical upward gust, the aircraft climbes up about 5 m. During the climb, the wing tip deflection decreases slightly. After the gust, the altitude of the aircraft begin to drop, and the effective angle of attack and airspeed of the aircraft increases during the descent. The dihedral and wing tip deflection of the wing also increase accordingly.

As the bending deformation of the wing increases, the pitch moment of inertia and the longitudinal static stability margin of the aircraft become larger, and the phugoid mode change from stable to unstable. The amplitudes of altitude, pitch angle and airspeed increase with the number of oscillations. It can be seen that in each oscillation period, the bending deformations of the wing decrease when the aircraft climbs, and increases when it descends. When the aircraft is at the lowest point of the oscillation period, the bending deformations of the wing reach the maximum.

As the oscillations continue, the altitude of the aircraft gradually decreases, and the amplitude of altitude and wingtip deflection gradually increases. After 6 oscillations, the altitude droppes by about 20 m, and the wingtip deflection reaches 12 m, about 30% of the half-wing span.

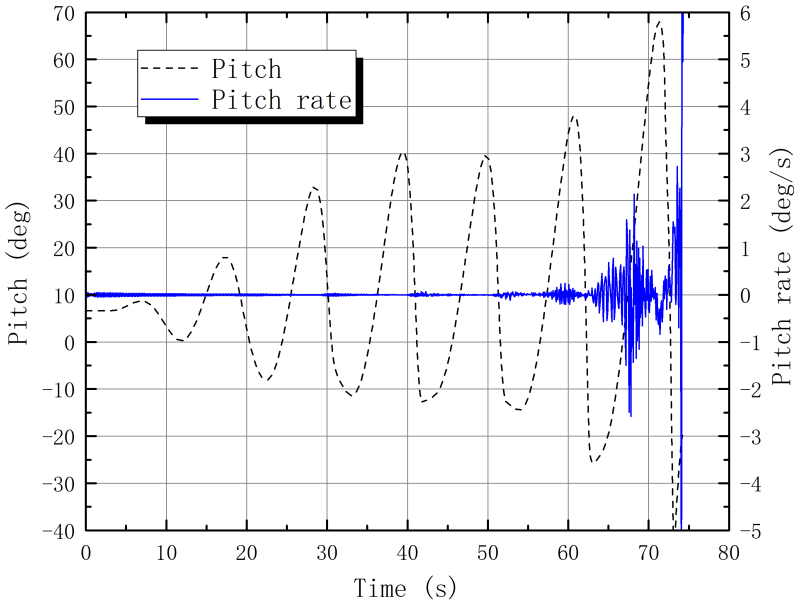

Figure 11 – Pitch angle and pitch angle rate v.s. time

It can be seen from figures 11-12 that due to the unstable phugoid mode, the amplitude of the pitch angle of the aircraft gradually increases. In the first three oscillations, the amplitude of each oscillation almost doubles, but the pitch angle rate is very small and never exceeding $\pm 0.1^\circ$/s. After 6 oscillations, the range of pitch angle change is expanded to -25°~50°, and the pitch angular rate also begin to fluctuate sharply, reaching $\pm 2^\circ$/s. In the last oscillation before disintegration, the pitch angle of the aircraft at the highest point reaches 68°. Then, it dived down at a pitch angle of -40°, with an airspeed approaching 30 m/s, approximately 2.5 times of the cruising speed. There are severe jitters at the same time, the pitch angle speed exceeded $\pm 5^\circ$/s, and the overload of the wingtip exceeded ± 10 g, indicating that the wing is about to break up.

In this section, by establishing a time-domain nonlinear aeroelastic and flight dynamics coupling model with the same geometric shape, structure, and mass characteristics as the "Helios" HP03-2 aircraft, it is calculated and interpreted that it produces a large and continuous upward deformation after being disturbed by gusts in flight, which leads to rapid divergence of the phugoid mode and finally disintegration in the air. The main characteristics of the aircraft's motion obtained are completely consistent with the phenomenon described in the accident investigation report.

By the modeling and calculation of the motion of "Helios" HP03-2 aircraft in flight after being disturbed by gusts, combined with the research in the previous section, it is shown that the fundamental reason for the disintegration of the aircraft is the reduction of stability of phugoid mode of the aircraft, which

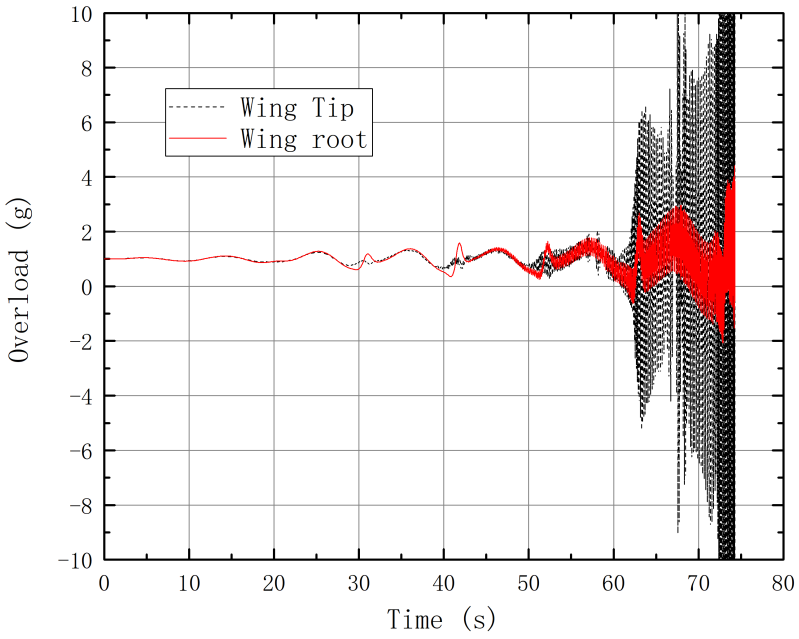

Figure 12 – Overloads of wing root and wing tip v.s. time

is the result of relatively large bending deformation of the wings caused by the unreasonable load distribution of the aircraft.

4. Concluding Remarks

A comprehensive analytical framework for the coupled flight dynamics and nonlinear aeroelasticity of highly flexible aircraft has been presented.

The present framework accounts for realistic design elements including arbitrary structural shapes and properties, concentrated masses, multiple thrusts and control surfaces, and unsteady aerodynamics. With excellent agreements reached, the accuracy, stability, efficiency and reliability of the presented framework and its corresponding computing codes are validated. It is adaptive and easy to accommodate with other models, and can be used for complete aircraft analyses in the conceptual and preliminary design phases, including the quick linear and nonlinear trim, aerodynamic load estimation, stability assessment, as well as linear and nonlinear time-domain response simulations.

5. Contact Author Email Address

Mailto: zhangchi_npu@mail.nwpu.edu.cn

6. Copyright Statement

References

[1] Jesús Gonzalo, Deibi López, Diego Domínguez, Adrián García, and Alberto Escapa. On the capabilities and limitations of high altitude pseudo-satellites. *Progress in Aerospace Sciences*, 98:37–56, 2018.

[2] Thomas E Noll, John M Brown, Marla E Perez-davis, Stephen D Ishmael, Geary C Tiffany, and Matthew Gaier. Investigation of the helios prototype aircraft mishap. Technical Report January, NASA, 2004.

[3] Amir Hossein Modaress-Aval, Firooz Bakhtiari-Nejad, Earl H. Dowell, David A. Peters, and Hossein Shahverdi. A comparative study of nonlinear aeroelastic models for high aspect ratio wings. *Journal of Fluids and Structures*, 85:249–274, 2019.

[4] Carlos E.S. Cesnik, Rafael Palacios, and Eric Y. Reichenbach. Reexamined structural design procedures for very flexible aircraft. *Journal of Aircraft*, 51(5):1580–1591, 2014.

[5] Yinan Wang, Andrew Wynn, and Rafael Palacios. Nonlinear aeroelastic control of very flexible aircraft using model updating. *Journal of Aircraft*, 55(4):1551–1563, 2018.

[6] M. M. Rezaei, M. Behzad, H. Haddadpour, and H. Moradi. Aeroelastic analysis of a rotating wind turbine blade using a geometrically exact formulation. *Nonlinear Dynamics*, 89(4):2367–2392, 2017.

[7] M.J. Patil, D.H. Hodges, and C.E.S. Cesnik. Limit-cycle oscillations in high-aspect-ratio wings. *Journal of Fluids and Structures*, 15(1):107–132, jan 2001.

[8] Himanshu Shukla and Mayuresh J. Patil. Nonlinear state feedback control design to eliminate subcritical limit cycle oscillations in aeroelastic systems. *Nonlinear Dynamics*, 88(3):1599–1614, 2017.

[9] Mayuresh J. Patil and Dewey H. Hodges. Flight dynamics of highly flexible flying wings. *Journal of Aircraft*, 43(6):1790–1799, 2006.

[10] Carlos E.S. Cesnik and Weihua Su. Nonlinear aeroelastic modeling and analysis of fully flexible aircraft. In *Collection of Technical Papers - AIAA/ASME/ASCE/AHS/ASC Structures, Structural Dynamics and Materials Conference*, volume 7, pages 4472–4498, 2005.

[11] Christopher M. Shearer and Carlos E.S. Cesnik. Nonlinear flight dynamics of very flexible aircraft. *Journal of Aircraft*, 44(5):1528–1545, 2007.

[12] Christopher M. Shearer and Carlos E.S. Cesnik. Trajectory control for very flexible aircraft. *Journal of Guidance, Control, and Dynamics*, 31(2):340–357, 2008.

[13] Weihua Su and Carlos E. S. Cesnik. Dynamic response of highly flexible flying wings. *AIAA Journal*, 49(2):324–339, 2011.

[14] Henrik Hesse and Rafael Palacios. Reduced-order aeroelastic models for dynamics of maneuvering flexible aircraft. *AIAA Journal*, 52(8):1717–1732, 2014.

[15] Joseba Murua, Rafael Palacios, and J. Michael R. Graham. Assessment of wake-tail interference effects on the dynamics of flexible aircraft. *AIAA Journal*, 50(7):1575–1585, 2012.

[16] Joseba Murua, Rafael Palacios, and J. Michael R. Graham. Applications of the unsteady vortex-lattice method in aircraft aeroelasticity and flight dynamics. *Progress in Aerospace Sciences*, 55:46–72, 2012.

[17] Martin R. Waszak and David K. Schmidt. Flight dynamics of aeroelastic vehicles. *Journal of Aircraft*, 25(6):563–571, jun 1988.

[18] Zhi Gang Wu and Chao Yang. Flight Loads and Dynamics of Flexible Air Vehicles. *Chinese Journal of Aeronautics*, 17(1):17–22, 2004.

[19] Chi Zhang, Zhou Zhou, and Pu Meng. Nonlinear static aeroelastic and trim analysis of highly flexible aircraft. In *31st Congress of the International Cuncil of the Aeronautical Sciences*, Belo Horizonte, 2018.

[20] Chi Zhang, Zhou Zhou, Xiaoping Zhu, and Pu Meng. Nonlinear static aeroelastic and trim analysis of highly flexible joined-wing aircraft. *AIAA Journal*, 56(12):4988–4999, 2018.

[21] M.A. Crisfield. *Non-linear Finite Element Analysis of Solids and Structures Volume 2: Advanced Topics*. JOHN WILEY & SONS, 1997.

[22] M. A. Crisfield. A consistent co-rotational formulation for non-linear, three-dimensional, beam-elements. *Computer Methods in Applied Mechanics and Engineering*, 81(2):131–150, 1990.

[23] K. J. Bathe and S. Bolourchi. Large displacement analysis of threedimensional beam structures. *International Journal for Numerical Methods in Engineering*, 14(7):961–986, 1979.

[24] A. Cardona and M. Geradin. A beam finite element nonlinear theory with finite rotations. *International Journal for Numerical Methods in Engineering*, 26(11):2403–2438, 1988.

[25] M. A. Crisfield, U. Galvanetto, and G. Jelenić. Dynamics of 3-d co-rotational beams. *Computational Mechanics*, 20(6):507–519, 1997.

[26] M. A. Crisfield and J. Shi. An energy conserving co-rotational procedure for non-linear dynamics with finite elements. *Nonlinear Dynamics*, 9(1-2):37–52, 1996.

[27] Ricardo De Frias Lopez. A 3d finite beam element for the modelling of composite wind turbine wings, 2013.

[28] David A. Peters, Swaminathan Karunamoorthy, and Wen Ming Cao. Finite state induced flow models. Part I: Two-dimensional thin airfoil. *Journal of Aircraft*, 32(2):313–322, 1995.